Inorganic Chemistry

Article

pubs.acs.org/IC

# Easy Synthesis of High-Purity $BiFeO_3$ Nanoparticles: New Insights Derived from the Structural, Optical, and Magnetic Characterization

José Luis Ortiz-Quiñonez,[†] David Díaz,*,[†] Inti Zumeta-Dubé,[†] Humberto Arriola-Santamaría,[†]
Israel Betancourt,[‡] Patricia Santiago-Jacinto,[§] and Noel Nava-Etzana[∥]

[†]Departamento de Química Inorgánica y Nuclear, Facultad de Química, [‡]Instituto de Investigaciones en Materiales, and [§]Instituto de Física, Universidad Nacional Autónoma de México, Ciudad Universitaria, Coyoacán CP 04510, Mexico City, Mexico

[∥]Instituto Mexicano del Petróleo, Eje Central Lázaro Cárdenas Norte 152, San Bartolo-Atepehuacan, G. A. Madero, CP 077730, Mexico City, Mexico

Supporting Information

**ABSTRACT:** Synthesis of high-purity $BiFeO_3$ is very important for practical applications. This task has been very challenging for the scientific community because nonstoichiometric $Bi_xFe_yO_z$ species typically appear as byproducts in most of the synthesis routes. In the present work, we outline the synthesis of $BiFeO_3$ nanostructures by a combustion reaction, employing tartaric acid or glycine as promoter. When glycine is used, a porous $BiFeO_3$ network composed of tightly assembled and sintered nanocrystallites is obtained. The origin of high purity $BiFeO_3$ nanomaterial as well as the formation of other byproducts is explained on the basis of metal−ligand interactions. Structural, morphological, and optical analysis of the intermediate that preceded the formation of porous $BiFeO_3$ structures was accomplished. The thorough characterization of $BiFeO_3$ nanoparticles (NPs) included powder X-ray diffraction (XRD); scanning electron microscopy (SEM) and high resolution transmission electron microscopy (HRTEM); thermogravimetric analysis (TGA); UV−vis electronic absorption (diffuse reflectance mode), Raman scattering, Mössbauer, and electron paramagnetic resonance (EPR) spectroscopies; and vibrating sample magnetometry (VSM). The byproducts like $\beta$-$Bi_2O_3$ and 5 nm $Bi_2Fe_4O_9$ NPs were obtained when tartaric acid was the promoter. However, no such byproducts were formed using glycine in the synthesis process. The average sizes of the crystallites for $BiFeO_3$ were 26 and 23 nm, for tartaric acid and glycine promoters, respectively. Two band gap energies, 2.27 and 1.66 eV, were found for $BiFeO_3$ synthesized with tartaric acid, obtained from Tauc's plots. A remarkable selective enhancement in the intensity of the $BiFeO_3$ $A_1$ mode, as a consequence of the resonance Raman effect, was observed and discussed for the first time in this work. For glycine-promoted $BiFeO_3$ nanostructures, the measured magnetization ($M$) value at 20 000 Oe (0.64 emu $g^{-1}$) was ∼5 times lower than that obtained using tartaric acid. The difference between the $M$ values has been associated with the different morphologies of the $BiFeO_3$ nanostructures.

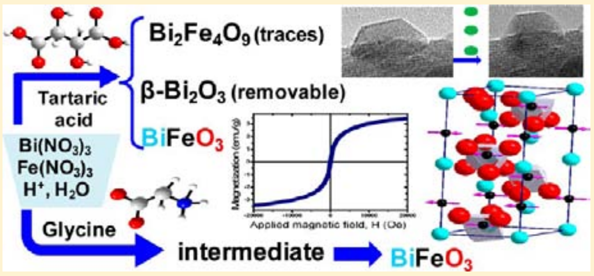

## 1. INTRODUCTION

Bismuth ferrite ($BiFeO_3$), in its bulk form, is an antiferromagnetic, ferroelectric, and multiferroic material. It has an antiferromagnetic Néel temperature of 643 K and a ferroelectric Curie temperature of 1103 K.[1] Due to these exceptional physical features, great interest has been raised for this material in several fields of science and technology. In the form of thin films, this compound has many potential device applications exploiting its photovoltaic,[2,3] ferroelectric, piezoelectric, or magnetoelectric capabilities, as well as in spintronics.[4] Probably, that is why the thin film has been the most studied and applied form of $BiFeO_3$. For example, in 2007 Fujitsu introduced a new ferroelectric random access memory (FRAM) for a 90-nm technology node, based on a 5% Mn-doped $BiFeO_3$ thin film.[5] For the aforementioned applications, the purity of $BiFeO_3$ was very critical because the reaction byproducts could modify the magnetic properties.[6]

Nanoparticulated $BiFeO_3$ constitutes a very important material that has had less attention paid to it by the scientific community. Being a semiconductor with the absorption edge in the visible region, $BiFeO_3$ NPs have been successfully tested in the degradation of rhodamine B,[7] methyl orange,[8,9] methylene blue,[10] and bisphenol A.[11] Also, $BiFeO_3$ NPs have been considered for the production of hydrogen through solar water splitting.[12] For this kind of surface reaction on $BiFeO_3$ NPs, it is important to quantify the remaining $NO_3^{1-}$ or other anions that could be adsorbed onto the NP surface, thus changing its surface reactivity.[11] Furthermore, the impurities or amorphous phases could modify the electron−hole recombination kinetics, affecting the photocatalytic efficiency of $BiFeO_3$. Therefore, developing methods for synthesizing high purity $BiFeO_3$ NPs is highly desirable.

In a review by Silva et al.,[13] a list of secondary phases ($Bi_{25}Fe_2O_{39}$, $Bi_{25}FeO_{40}$, $Bi_2Fe_4O_9$, $Bi_{46}Fe_2O_{72}$, $Bi_{36}Fe_{24}O_{57}$), which are common byproducts in the synthesis of $BiFeO_3$ or

**Received:** March 13, 2013
**Published:** August 22, 2013

dx.doi.org/10.1021/ic400627c | *Inorg. Chem.* 2013, 52, 10306−10317

doped $BiFeO_3$ NPs, were put together after consulting at least 20 papers; these were obtained by a conventional solid state reaction or sol−gel methods. Other additional publications, not included in that review, have also reported the formation of some of those secondary phases,[7,14−16] an amorphous shell of 1−2 nm thickness around the $BiFeO_3$ NPs,[17] $Bi_2O_3$,[7,18,19] and 5% of an unidentified impurity phase.[13] Lebeugle et al. have pointed out that the $Bi_{25}Fe_2O_{39}$ impurity is responsible for the weak ferromagnetism at low temperature in polycrystalline $BiFeO_3$.[20] However, we found two publications in which few samples synthesized under specific conditions have XRD patterns of pure $BiFeO_3$.[21,22]

Until now, the most comprehensive characterization for the $BiFeO_3$ NPs has been documented by Park et al.[23,24] They have demonstrated the dependence of magnetic properties on the size of NPs. However, there were no band gap estimations, nor TGA experiments, to find out residues from the reagents which can modify the catalytic, magnetic, or optical properties of the NPs. While EPR measurements were not performed, their reported Raman measurements were made with just one laser source of 514.5 nm.[24] In the literature, there are some reports which show the Raman scattering spectrum of $BiFeO_3$,[25−34] but only two of them[26,34] measured the two-phonon overtones using resonance Raman scattering; none of them reported the band gap value either of bulk single crystal or of thin films. When the frequency of the laser beam is close to the frequency of an electronic transition, scattering enhancements have been observed.[35] This phenomenon is called resonance Raman scattering, where intense overtones are allowed. The increase in intensity from resonance enhancement can be understood by studying the Kramer−Heisenberg−Dirac (KHD) expression for the polarizability, comprehensively discussed in ref 35. So far, for $BiFeO_3$, there are no reports about the relationship of overtones and electronic transitions induced by laser sources.

Da Silva et al.[36] have reported the preparation of $BiFeO_3$ NPs via mechanochemical method employing an $\alpha$-$Fe_2O_3$/$Bi_2O_3$ mixture, but the size distribution of their NPs was relatively broad (ranged from about 5 to 40 nm), and an amorphous phase was detected by XRD. However, the maximum magnetic susceptibility at 20 K in the zero field cooling (ZFC) curve, reported by Da Silva et al., differs from that reported at 50 K by Prado et al.[37] and that obtained at 85 K by Park et al.[23,24] At the present, the reported band gap energy values for $BiFeO_3$ NPs and thin films are contradictory with regard to the expected qualitative dependence on the material dimensions (see Table S1).[8−10,25,38−49] It should be expected that the smaller the NPs the higher the band gap energy value, but the reported values do not show this trend. In the particular case of $BiFeO_3$ NPs, there is no agreement in theoretical considerations whether the electronic transitions are direct or indirect, see Table S1. This fact might introduce discrepancies among the experimentally reported band gap values.

The main objectives of the present research are to synthesize, purify, and characterize $BiFeO_3$ NPs, as well as the impurities (even at trace levels), with a wide variety of spectroscopic, structural, morphological, thermal, and magnetic techniques. We developed an easy method to obtain high purity $BiFeO_3$ nanocrystals at relatively low temperatures. This process is straightforward, simple, energy-saving, and cost-effective. An integral discussion about the role of glycinate ion as ligand, which has the same affinity constant for $Fe^{3+}$ and $Bi^{3+}$ ($\log K = 10$)[50,51] and slightly lower for $H^+$ ($\log K = 9.57$),[51] was accomplished. After a thorough characterization of the $BiFeO_3$ NPs by powder XRD, SEM, HRTEM, TGA, VSM, and UV−vis electronic absorption, Raman scattering, Mössbauer, and EPR spectroscopies, we obtained very interesting experimental results and offer consistent interpretations of the physicochemical properties of these ferrite NPs.

## 2. EXPERIMENTAL SECTION

The reagents used in the synthesis were bismuth nitrate pentahydrate ($Bi(NO_3)_3{\cdot}5H_2O$, Aldrich, > 98%), iron nitrate nonahydrate ($Fe(NO_3)_3{\cdot}9H_2O$, J.T. Baker, 99.6%), L-(+)-tartaric acid ($C_4H_6O_6$, Alfa Aesar, 99%), glycine ($H_2NCH_2COOH$, Aldrich, 99%), diluted nitric acid ($HNO_3$, J.T. Baker, 64%), and glacial acetic acid ($CH_3COOH$, J.T. Baker, 99.9%).

A typical preparation process used to obtain the precursors for the synthesis of $BiFeO_3$ NPs is the following: 0.004 mol of $Bi(NO_3)_3{\cdot}5H_2O$, 0.004 mol of $Fe(NO_3)_3{\cdot}9H_2O$, and 0.008 mol of L-(+)-tartaric acid or glycine were dissolved in a mixture of 40 mL of deionized water and 2.8 mL of $HNO_3$ at 64%, under magnetic stirring at room temperature. In each reaction, only one organic species (either tartaric acid or glycine) was used to complex $Bi^{3+}$ and $Fe^{3+}$ cations in aqueous solution. The mixture was heated until all solvent was evaporated, and a combustion reaction took place. In the reaction, the organic species was the reducing agent, and the $NO_3^{1-}$ was the oxidizing agent. The brown powder obtained using tartaric acid was heated in a furnace at 500 °C in air for 1 h, and then it was washed with water followed by $CH_3COOH$ at 65 °C to remove the $Bi_2O_3$. The powder obtained using glycine was annealed in air at 350 °C for 1 and then at 500 °C for 1 h in addition.

The measurements of the electronic absorption spectra using the diffuse reflectance technique were made in a UV−vis spectrophotometer (Ocean Optics CHEM-2000), equipped with a double-way optic fiber, coupled to a PC. The powder XRD patterns were collected in a Siemens D5000 diffractometer using a Cu source (K$\alpha$, $\lambda = 1.5406$ Å). The HRTEM observation was carried out in a Philips Tecnai F30 microscope operated at 300 KeV and equipped with a Gatan Image Filter to perform the EELS study. HRTEM images were processed using the Digital Micrograph 1.2 software. The SEM images were obtained in a field emission scanning electron microscope, JSM-7600F, from JEOL, with a secondary electron detector. The Raman scattering spectra were measured in a Horiba spectrometer, equipped with 3 laser sources ($\lambda = 532$, 633, and 785 nm), and a Synapse CCD detector with thermoelectric cooling at −75 °C.

The magnetic hysteresis loops ($M$−$H$) were measured in a vibrating sample magnetometer (VSM-VersaLab, 30000 Oe), at room temperature. The magnetic susceptibility at different temperatures was measured in a superconducting susceptometer MPMS-5s, Quantum Design. The thermograms were recorded on a TGA Q5000 V3.10 Build 258 equipment, brand TA, in modulated mode, using a heating ramp of 5 °C/min. The Mössbauer spectrometer (Wissel-Electronik) with a $^{57}Co$ source, embedded in a Rh matrix, with activity of 925 MBq (25 mCi), was operated at 300 and 77 K. The spectra fittings were made with the NORMOS software. EPR spectra were recorded on a Bruker equipment (Elexsys E 500).

## 3. RESULTS AND DISCUSSION

### 3.1. X-ray Powder Diffraction.

*a. $BiFeO_3$ NPs Synthesized Using Tartaric Acid as Ligand.* Typical X-ray powder diffraction (XRD) patterns of the $BiFeO_3$ obtained using tartaric acid before and after its purification are shown, Figure 1. The peaks in Figure 1a belong to rhombohedral $BiFeO_3$ (PDF 861518), and the main byproducts were $\beta$-$Bi_2O_3$ (PDF 781793)[53] as indicated with the blue arrows, and the $\alpha$-$Bi_2O_3$ phase (PDF 761730) as indicated with the asterisk.

Figure 1b shows an XRD pattern of the $BiFeO_3$ powder, taken after washing with $CH_3COOH$ to remove the bismuth oxide impurities. Usually these oxides were removed with $HNO_3$,[18] a strong acid, which could dissolve $BiFeO_3$. For the

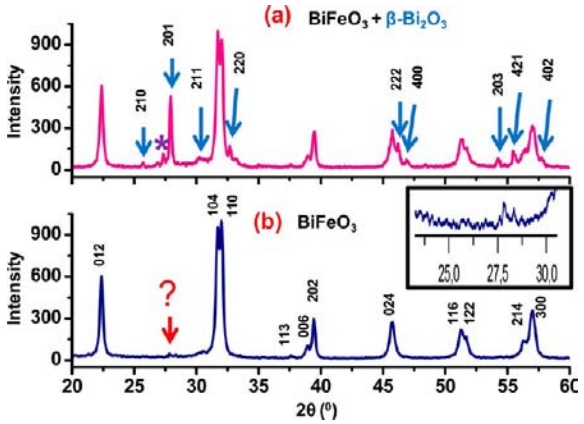

**Figure 1.** X-ray powder diffraction patterns of $BiFeO_3$ synthesized using tartaric acid as ligand (a) before and (b) after the treatment with $CH_3COOH$ to remove the byproducts: $\beta$-$Bi_2O_3$ and $\alpha$-$Bi_2O_3$. The inset is a zoom-in around the peak at $2\theta = 27.90°$.

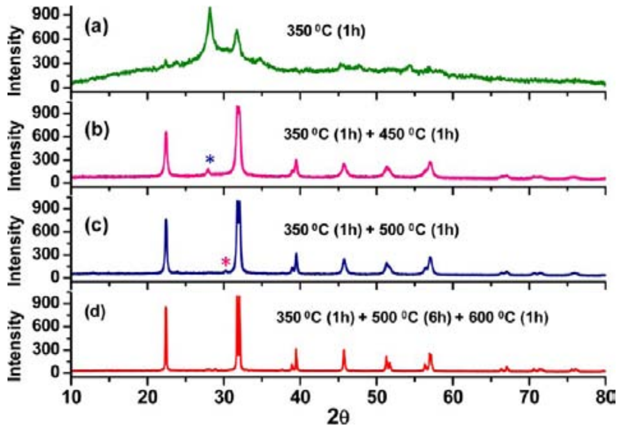

**Figure 2.** XRD patterns of (a) precursor (intermediate) and (b−d) the $BiFeO_3$ NPs, obtained using glycine as ligand, annealed at different temperatures and times. The asterisk in part c corresponds to the byproduct $(BiO)_2CO_3$.

first time, a weak acid, $CH_3COOH$, was used for purifying purposes. The average crystallite size of $BiFeO_3$ nanostructures was 26 nm, determined by means of the Scherrer equation, using the (012) and (024) planes only. The relatively small peak located at $2\theta = 27.91°$, indicated with the question mark and shown in the inset, does not belong to $BiFeO_3$. This peak matches with the most intense reflection of $Bi_{24}Fe_2O_{39}$, located at $2\theta = 27.97°$ (PDF 420201). The signal at $2\theta = 27.97°$ is also close to the most intense peak of $Bi_2Fe_4O_9$ (PDF 250090), a common byproduct, which is located at $2\theta = 28.20°$ (PDF 250090). Recently, Kothai et al.[54] reported the $Bi_{24}FeO_{39}$ impurity during the synthesis of $BiFeO_3$ NPs based on a small peak located at $2\theta = 27.9°$. Considering that an amount of bismuth was consumed for the $\beta$-$Bi_2O_3$ formation, we propose $Bi_2Fe_4O_9$ as the most probable byproduct. In section 3.3 and Figure 6, there is a further discussion about the question mark issue.

We suggest the following pathway to explain the formation of the bismuth oxide phases as byproducts. In Bi(III) acidic aqueous solutions, intramolecular polycondensation of the hydrated ion takes place; leading to polynuclear cationic species such as $[Bi_6O_4(OH)_4]^{6+}$, $[Bi_6O_5(OH)_3]^{5+}$, and $[Bi_9(\mu_3\text{-}O)_8(\mu_3\text{-}OH)_6]^{5+}$.[55−60] These polynuclear species can form clusters and then, under thermal treatment, decompose into the $\alpha$- and $\beta$-$Bi_2O_3$ phases. This is the first time that the formation of the byproducts $\alpha$- and $\beta$-$Bi_2O_3$ could be associated with these polynuclear species in the synthesis of $BiFeO_3$ NPs.

The anion of the L-(+)-tartaric acid and $Bi^{3+}$ form polymeric chains with a nine-coordinate bismuth center ($BiO_9$).[51,61] However, the tartrate anion does not have the same affinity for $Bi^{3+}$ and $Fe^{3+}$.[51,62,63] Consequently, the two cations do not get homogeneously distributed in the polymeric chains in the precursor solutions. This could be a new possible explanation for the formation of $Bi_2O_3$ and $Bi_2Fe_4O_9$ byproducts, or a different Bi/Fe atomic ratio from 1:1 in the $BiFeO_3$ NPs, obtained during the combustion reaction.

*b. $BiFeO_3$ NPs Synthesized Using Glycine as Ligand.* Figure 2 shows the XRD patterns of $BiFeO_3$ NPs at different stages of the heating process. In Figure 2a, several peaks do not belong to the $BiFeO_3$ phase, and the most intense peak is located at $2\theta = 28.17°$. Formation of an amorphous phase can also be observed from the curvature of the baseline. Although the most intense peak could not be directly assigned to any specific species, the Raman spectrum of this material only shows signals corresponding to $BiFeO_3$ (see Figure S1) suggesting that the sample is mainly constituted by that phase and probably an oxygen deficient bismuth ferrite. The presence of oxygen deficient bismuth ferrite could be due to the formation of combustion gases (NO, $NO_2$, CO, $CO_2$, and $H_2O$) that take up the available oxygen, and the capability of $CO_2$ and $H_2O$ to remove molecular oxygen. SEM analysis revealed the generation of a porous framework of nanocrystals smaller than 10 nm in this intermediate (see Figure S2a). It is noteworthy to mention that the crystallites forming this framework are preferentially aligned in the porous assemble (see Figure S2c).

From the ATR-FTIR spectrum in Figure S4, the bands at 846 and 1379 $cm^{-1}$ confirm the presence of $(BiO)_2CO_3$, and the remaining bands agree with the $NO_3^{1-}$ group coordinated to $Bi^{3+}$.[64] After heating this sample for one additional hour at 450 °C (Figure 2b), all the peaks correspond to the $BiFeO_3$ phase, except that indicated with the asterisk at $2\theta = 27.96°$.

When the sample was heated at 350 °C for an hour and then at 500 °C for an additional hour (Figure 2c), all the prominent peaks that appeared in its XRD pattern correspond to $BiFeO_3$, except the weak peak appearing at $2\theta = 30.26°$ marked by the asterisk in Figure 2c, which was associated to the $(BiO)_2CO_3$ phase, as has been reported previously by Taylor et al.[65] The presence of $(BiO)_2CO_3$ was also confirmed by its ATR-FTIR spectrum (see Figure S4). The average crystallite size of the $BiFeO_3$ (Figure 2c) was about 23 nm, determined by the Scherrer equation, only using the (012) and (024) planes. The $\alpha$- and $\beta$-$Bi_2O_3$ byproducts were not detected by XRD, so the treatment with $CH_3COOH$ was not necessary. This is the main difference observed between the use of glycine or tartaric acid for the synthesis. The reasons for this pathway differentiation might be the following: (a) There is a homogeneous distribution of the Fe(III)−glycine and Bi(III)−glycine complexes due to the similar affinity constants that the glycinate anion has for the cations ($Fe^{3+}$, $Bi^{3+}$, and $H^+$).[50,51] (b) The glycinate anion competes with $NO_3^{1-}$ and interrupts the formation of the 3D networks of bismuth oxide clusters, like $[Bi_6O_4(OH)_4(NO_3)_6(H_2O)]\cdot H_2O$.[71] The latter forms bismuth oxide when decomposed under annealing. (c) The $pK_a$ of the carboxylic group of glycinate ion (2.34) is lower than that of tartaric acid (2.95 and 4.25).

In order to evaluate the thermal stability of the $BiFeO_3$ NPs, they were heated as indicated in Figure 2d. The heating process resulted in a size increase to about 67 nm (calculated using the Scherrer equation). The peak that corresponds to the $(BiO)_2CO_3$ phase was no longer detected after the annealing process as it decomposes between 350 and 650 °C.[65] The high purity of the obtained $BiFeO_3$ powder observed by XRD was corroborated by TGA analysis; the results are presented and discussed in Figures S5 and S6.

### 3.2. Scanning Electron Microscopy (SEM).

*a. $BiFeO_3$ NPs Synthesized Using Tartaric Acid as Ligand.* For further characterization, the $BiFeO_3$ NPs were analyzed by SEM, and a typical image is presented in Figure 3. It is clear that the NPs are aggregated and have sizes smaller than 50 nm, which agree with their XRD results. The Bi/Fe ratio was determined by the SEM–EDS technique. These ratios were measured in two different zones of an area of about 1 $\mu m^2$ each, where 0.91 and 1.04 should be 1 in the ideal case; these values are acceptable within the accuracy of the technique and comparable with previous works. For example, for the $BiFeO_3$ films deposited at low oxygen pressures, the ratio was calculated to be about 1.2:1 using XPS measurements.[49]

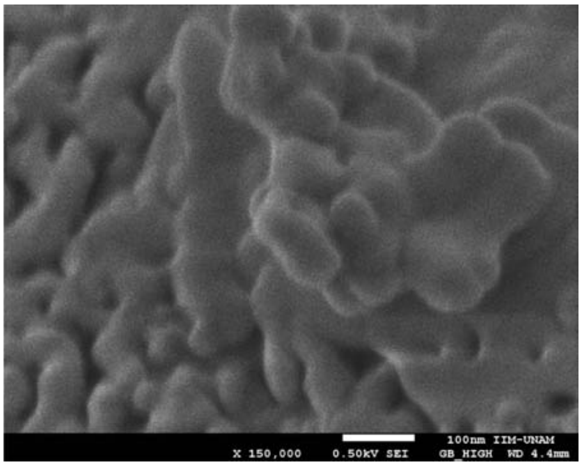

**Figure 3.** Typical SEM image of the aggregated $BiFeO_3$ NPs, prepared using tartaric acid. The scale bar is of 100 nm.

*b. $BiFeO_3$ NPs Synthesized Using Glycine as Ligand.* In the images of $BiFeO_3$ NPs analyzed by SEM, it looks like a highly porous network instead of simple nanoparticle aggregates, as can be seen in Figure 4. The pore sizes ranged from several micrometers to submicrometer dimensions, and these holes have irregular shapes. The pores are created due to the fast release of combustion gases. This structure is derived from the previously formed intermediate (Figure S2a,b). In the literature we can find that, during the combustion reaction between glycine and metal nitrates, the temperature inside the flame is increased to a maximum between 1100 and 1450 °C,[52,66] rising from 150 to 1285 °C in less than 4 s;[52] consequently, several gases are abruptly released (NO, $NO_2$, CO, $CO_2$, $NH_3$, and $H_2O$),[52,67] and products with microporous structures are formed.[7,68−70] Hwang et al. have reported a combustion reaction between metal (Ni, Zn, and Fe) nitrates and glycine studied by differential scanning calorimetry (DSC) in which the curve showed a sharp exothermic peak at ~178 °C with an area of −520 cal/g.[52] This energy can be taken by the released gases to create those microporous structures observed in refs 7, 68, 69, and 70. It can be inferred from the experiments in ref 52 that 64% of the sample weight evolves as gases in about 0.25 s, while the microporous structure is formed.

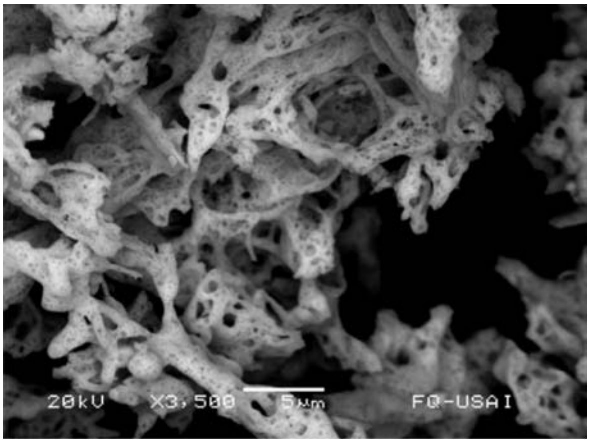

**Figure 4.** SEM image of the $BiFeO_3$ porous network prepared using glycine in the synthesis methodology. The scale bar is of 5000 nm.

The theoretical values for the atomic percentage of Bi, Fe, and O in $BiFeO_3$ are 20, 20, and 60, respectively. These values are close to those obtained experimentally by SEM-EDS (19 ± 2%, 20 ± 4%, and 60 ± 4%).

### 3.3. High Resolution Transmission Electron Microscopy (HRTEM).

*a. $BiFeO_3$ NPs Synthesized Using Tartaric Acid as Ligand.* An HRTEM image of one $BiFeO_3$ NP is shown in Figure 5a. This NP has an ellipsoidal shape and approximate dimensions of $14 \times 19$ $nm^2$. The interplanar spacing observed in this micrograph is 3.92 Å and corresponds to the {012} $BiFeO_3$ family planes, that is, the first peak shown in Figure 1b. Figure 5b corresponds to the fast Fourier transform (FFT) of the selected area, in which the interplanar distances of the $BiFeO_3$ were identified. The reciprocal lattice simulated by the CaRIne software, viewed from the [14−2] zone axis, shown in Figure 5c, agrees well with the FFT of Figure 5b.

The only byproduct found in some HRTEM images was tiny NPs of about 5 nm size, as shown in Figure 6a. The FFT analysis of the zone marked by the red square in Figure 6a is presented in Figure 6b. The interplanar distance found was 3.2 Å. This distance matches with the interplanar distance associated to the very small peak indicated with the arrow in the diffractogram of Figure 1b, which means that these tiny NPs are possibly $Bi_2Fe_4O_9$.

The iron-rich $Bi_2Fe_4O_9$ impurity was possibly formed since a fraction of bismuth atoms were consumed in the formation of the $\beta$-$Bi_2O_3$ byproduct, keeping a small amount of Fe(III) in the reaction media. The $Bi_2Fe_4O_9$ byproduct had already been reported;[7,54,72,73] however, this is the first time that its size was determined, which is very important because at low temperatures the saturation magnetization of $Bi_2Fe_4O_9$ NPs increases as the size decreases.[74] Another relevant result obtained was that the tiny $Bi_2Fe_4O_9$ particles underwent a rearrangement of the crystalline structure through quasimelt states (structural instability) induced by the electron beam from the microscope,[75−77] as can be seen in the video in the Supporting Information. Da Silva et al.[36] prepared $BiFeO_3$ NPs via mechanochemical processing of an $\alpha$-$Fe_2O_3$/$Bi_2O_3$ mixture, and they highlighted the formation of small NPs with interplanar distance of 3.2 Å that were formed by a rapid

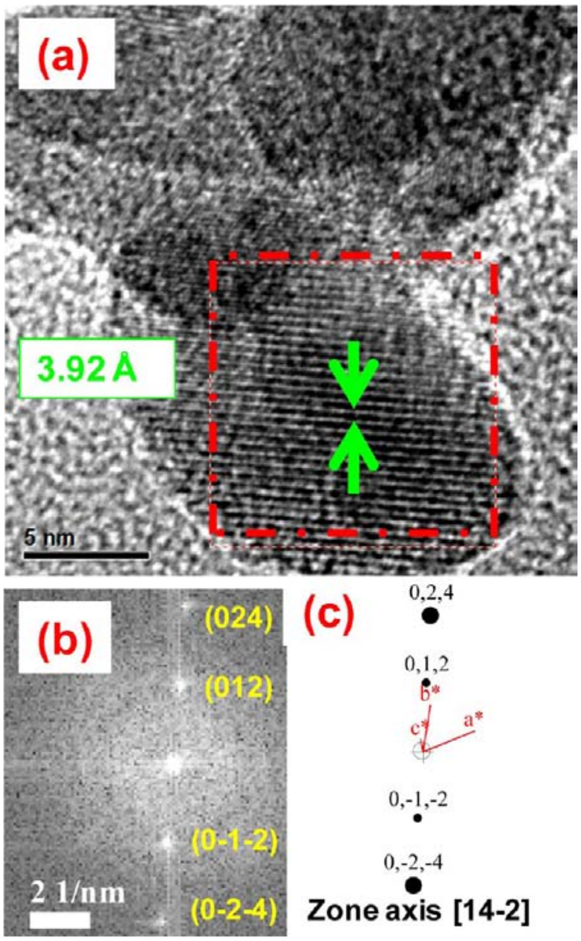

**Figure 5.** (a) Typical HRTEM image of one $BiFeO_3$ NP. (b) Fast Fourier transform of the squared area marked in part a. (c) Electron diffraction pattern simulated by CaRIne v. 3.1 for $BiFeO_3$.

crystallization reaction upon the electron irradiation during the course of HRTEM investigation. We suggest that what they saw in their HRTEM images was just structural instability but not formation of small NPs. A careful observation of the micrographs in ref 36 revealed the presence of those NPs even since $t = 0$ of electron-beam irradiation. In our case, the NPs' shape and facets notably changed as the lattice was rearranged by the electron beam interaction, including the so-called quasimelt states.

*b. $BiFeO_3$ Porous Network Synthesized Using Glycine as Ligand.* The HRTEM images of the $BiFeO_3$ NPs, obtained using the glycine methodology, are shown in Figure 7a, and at least in that image, their sizes are smaller than 60 nm and are aggregated. It can be seen that the $BiFeO_3$ NPs were tightly assembled and sintered giving support to the porous network presented in Figure 4. Hereafter, this $BiFeO_3$ NPs porous network will be called $BiFeO_3$−NPs−PNt. A closer view of one $BiFeO_3$ NP allowed us to determine the interplanar distances and confirm that it corresponds to the {104} family of planes, as can be seen in Figure 7b. Surrounding this $BiFeO_3$ NP, there are some unidentified small NPs, two of them indicated with the blue arrows.

**3.4. Comparison of the Electronic Absorption Spectra of the $BiFeO_3$ NPs Prepared Using Glycine and Tartaric Acid as Ligands.** The solid state UV−vis electronic absorption spectra of $BiFeO_3$ NPs at different annealing stages are shown in Figure 8. The sample with the portion of amorphous phase (shown in Figure 2a) has the less steep absorption edge in its absorption spectrum between 500 and 600 nm. This attribute is probably due to a variety of electronic environments around the iron(III) and bismuth(III) cations, possibly created by the remaining nitrates and carbonates (see Figure S3). Additionally, several other factors, including the amorphous phase, the smaller $BiFeO_3$ nanostructures, higher lattice strain, and the presence of other secondary phases, contribute to the resulting absorption profile. When the temperature is increased, the amount of nitrates decreases, and the percentage and the size of $BiFeO_3$ NPs increase while the lattice strain decreases, and hence make the absorption edge steeper. The nanostructures obtained at the longest annealing time are of largest in size, i.e., 67 nm, and have the most abrupt absorption edge. This can be explained since these nanostructures are the most crystalline and purest; they must have the smallest specific surface area and the highest crystalline order at the interparticle contact. This means less absorption contribution from the tails density of states. Taking into account that the heating treatment was performed in air atmosphere, these largest crystallites should have fewer oxygen vacancies.

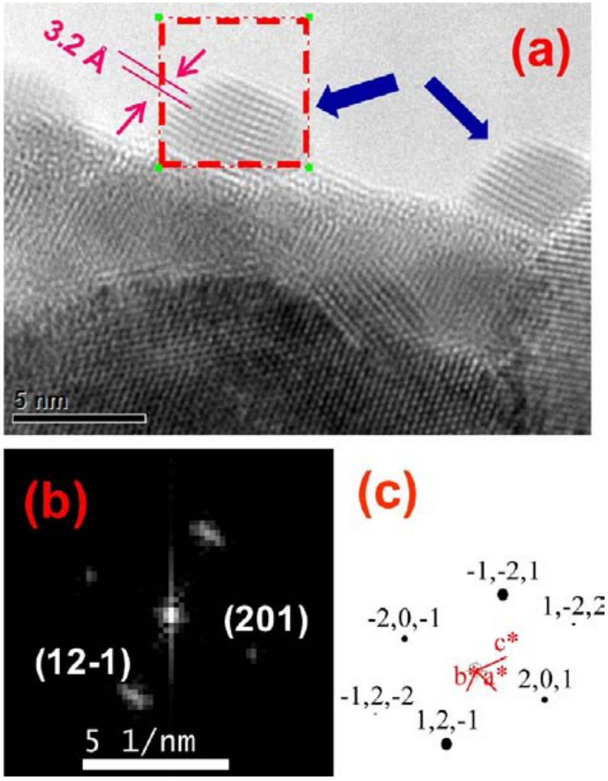

**Figure 6.** (a) HRTEM image of a $BiFeO_3$ sample where two NPs of the byproduct $Bi_2Fe_4O_9$ were identified. (b) Fast Fourier transform of the zone indicated with the red square in part a. (c) Electron diffraction pattern simulated by CaRIne v. 3.1 for $Bi_2Fe_4O_9$ using the zone axis [−234].

The spectrum corresponding to the $BiFeO_3$ NPs prepared using tartaric acid as ligand (curve a) has a profile very similar to that obtained using glycine (curve d), see Figure 8. This is in accordance with the very similar crystallite size of both samples (26 and 23 nm, respectively).

From the linear fit in the Tauc's plot, restricted to the energy range 2.17−2.36 eV (525−570 nm), a direct band gap of 2.27 eV is found for the $BiFeO_3$ nanostructures of 23 nm crystallite

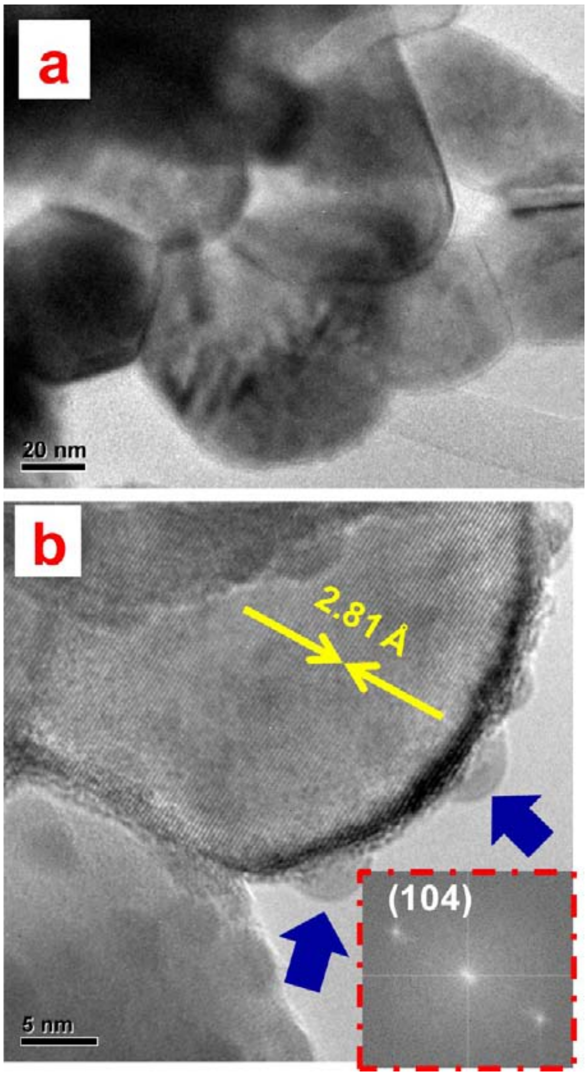

**Figure 7.** HRTEM images of (a) $BiFeO_3$−NPs−PNt and (b) unidentified small NPs surrounding a $BiFeO_3$ NP (two of them are indicated by the arrows); the inset in part b corresponds to the FFT. The corresponding XRD pattern of this sample is shown in Figure 2c.

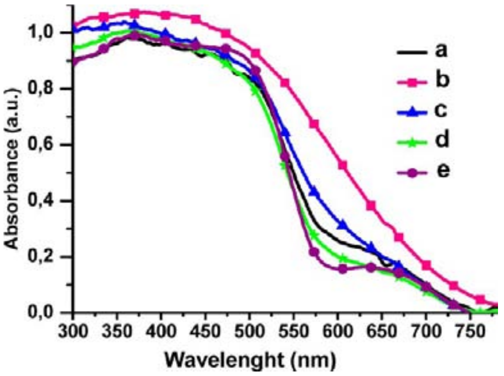

**Figure 8.** UV−vis absorption spectra collected by diffuse reflectance technique of $BiFeO_3$ NPs obtained using tartaric acid (a) and glycine (b, c, d, e) as ligands. The times and temperatures of heating were the following: (a) 500 °C, 1 h; (b) 350 °C, 1 h; (c) 350 °C, 1 h, + 450 °C, 1 h; (d) 350 °C, 1 h, + 500 °C, 1 h; (e) 350 °C, 1 h, + 500 °C, 6 h, + 600 °C, 1 h.

size (see Figure 9a). This direct band gap value is in-between those reported for $BiFeO_3$ nanostructures (1.8−2.5 eV)[9,25,78−80] that, at the same time, are red-shifted with respect to the bulk value (2.66−2.81 eV).[48,81−83] This effect has been explained on the basis of the fact that the typical electric dipole-allowed charge transfer excitations of bulk $BiFeO_3$ at 3.2 and 4.5 eV split into multiplets in nanoparticles with the net effect of moving the edge of the charge transfer band to lower energies.[25] That is a consequence of the strained nature of the nanostructures and the symmetry breaking in high surface to volume ratio systems.[25] The red shift of the absorption spectrum in $BiFeO_3$ has also been observed in other lattice-strained, doped, or surface-rich structures[78,84−86] and $BiFeO_3$ nanowires.[87]

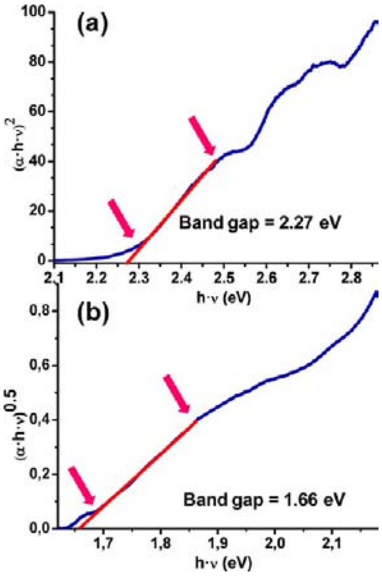

**Figure 9.** Tauc's plots to determine the band gap of the $BiFeO_3$ NPs, prepared using tartaric acid as ligand agent: (a) direct electron transition and (b) indirect electron transition.

Additionally, an indirect interband transition was detected at 1.66 eV in the same $BiFeO_3$ nanostructures of 23 nm crystallite size. It was derived from the Tauc's plot fit in the long tail-like part of the absorption spectrum, at wavelengths longer than 580 nm. The presence of both indirect and direct band gaps, in different energy ranges, has been observed by other authors in $BiFeO_3$ thin films.[48,88] In these cases the indirect transitions are located between 1.3 and 1.85 eV.[48,88] These reports are qualitatively in accordance with some theoretical studies where the existence of an indirect and a direct gap are predicted in the electronic structure of $BiFeO_3$.[4,72] The appearance of an indirect band gap has been also theoretically predicted in highly strained $BiFeO_3$.[85] In these reports,[4,72,85] the indirect gap is of smaller energy than the direct one.[89] According to Wang et al.,[89] the top of the valence band is composed by strong hybridization among O 2p, Bi 6p, and Fe 3d states, and the bottom of the conduction band is leading by Fe 3d states. Very similar band gap values, for direct and indirect transitions, were determined for $BiFeO_3$−NPs−PNt, see Figure S8.

### 3.5. Raman Scattering Spectroscopy.

*a. $BiFeO_3$ NPs Synthesized Using Tartaric Acid as Ligand.* $BiFeO_3$ belongs to the $R3c$ space group and the $C_{3v}$ point group. The irreducible representations obtained from group theory are the following: $4A_1\ (z, x^2 + y^2, z^2) + 5A_2\ (-) + 9E\ (x, y, x^2 - y^2, xy, xz, yz)$.[90]

However, the $A_2$ Raman modes are nonactive. In Figure 10 the measured Raman scattering spectra of the $BiFeO_3$ NPs, using three laser sources with different energy values, are presented. All bands in the spectra belong to the $BiFeO_3$ NPs.[25−34] Using the laser source of 532 nm (2.33 eV), which is just 0.06 eV higher than the band gap value of the NPs (2.27 eV, as presented in Figure 9a), three overtones were observed and that at 1255 $cm^{-1}$ is about 10 times more intense than the corresponding fundamental mode ($E_9$). The intensity of the overtone at 1255 $cm^{-1}$, using the laser source of 633 nm (1.96 eV), was very low because it only has enough energy for indirect electron transitions, which are about 1000 times less intense than the direct electronic transitions. When the laser source of 785 nm (1.59 eV) was used, the overtones were absent. These results confirm that electronic transitions take place under excitation with 532 nm laser radiation, as expected from the diffuse reflectance measurement, allowing the resonance effect.

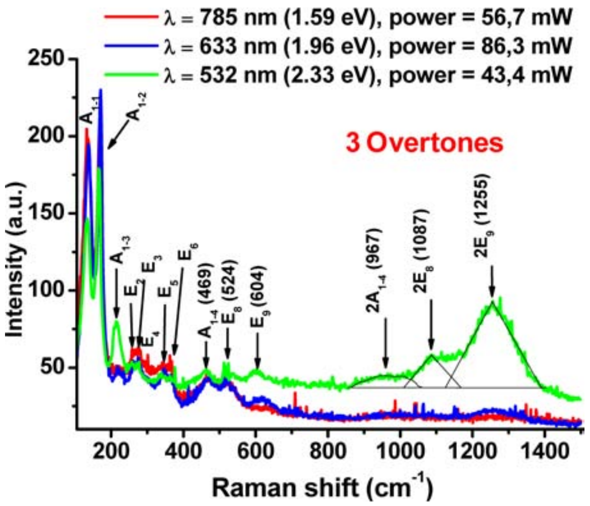

**Figure 10.** Raman spectra of the 26 nm $BiFeO_3$ NPs, prepared using the tartaric acid methodology, employing three different lasers as an excitation source.

Another remarkable finding was a notable intensity enhancement of the fundamental totally symmetric mode at 216 $cm^{-1}$ (see Figure 11a), labeled as $A_{1-3}$, when the laser source of 532 nm was used. It is important to mention that, in the resonance Raman phenomenon, the intensity enhancements observed in some vibrational modes are exclusively related to the atoms taking part in the electronic transition.[35] According to Porporati et al.,[91] Bi atoms only participate in the low wavenumber modes up to 167 $cm^{-1}$, while the oxygen motion strongly dominates in modes above 262 $cm^{-1}$ and Fe atoms are mainly involved in modes between 152 and 261 $cm^{-1}$. Moreover, first-principles calculation within generalized gradient approximation made by Liu et al.[92] and Wang et al.[89] concluded that the density of states at the lower conduction bands are conformed

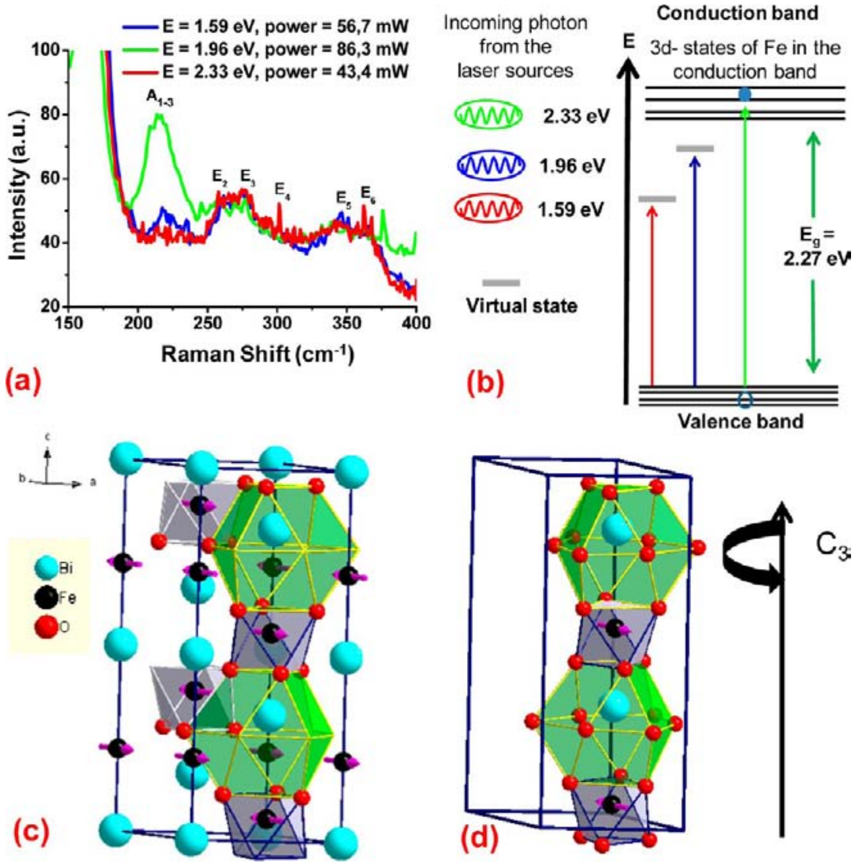

**Figure 11.** (a) Intensity enhancement of the $A_1$ Raman mode at 216 $cm^{-1}$ for $BiFeO_3$ using three laser sources of different energy (*E*), (b) sketch of the relationship between the energy of the laser sources used in the Raman measurements and the energy of the band gap, (c) sketch of the $BiFeO_3$ structure in the hexagonal unit cell using the atomic parameters obtained by Kubel et al.,[93] and (d) representative polyhedra around the $Fe^{3+}$ and $Bi^{3+}$ cations.

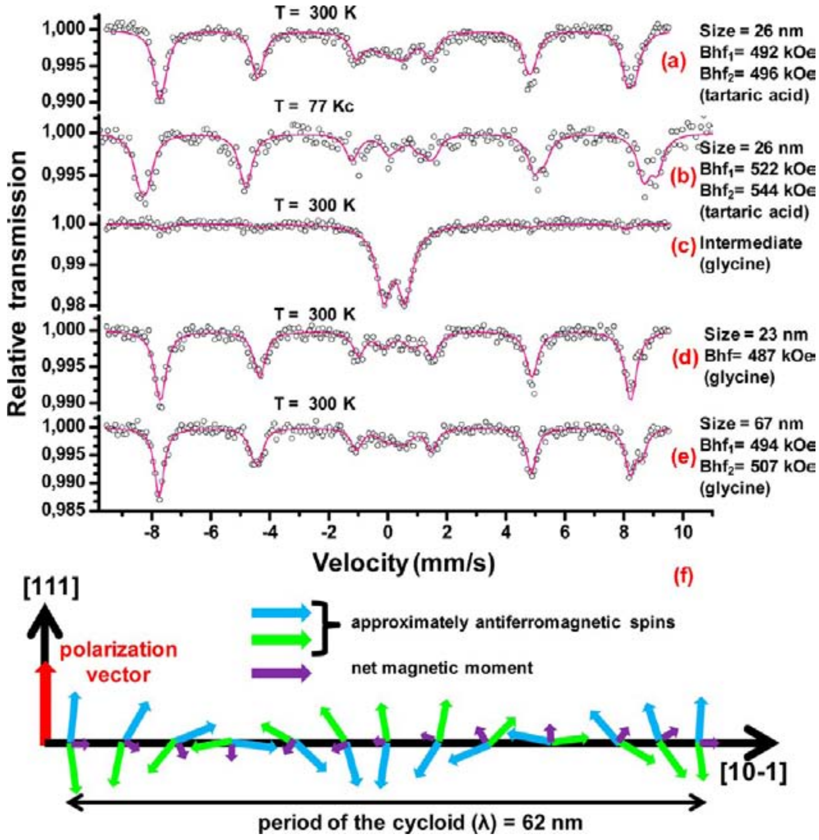

**Figure 12.** Mössbauer spectra of $BiFeO_3$ NPs of different sizes prepared using tartaric acid (a, b) and glycine (c, d, e) in the synthesis. Spectrum c corresponds to the intermediate. The spectra a, c, d, and e were measured at 300 K, while spectrum b was recorded at 77 K. (f) Schematic representation of the spin cycloid inspired from ref 4.

mostly by Fe-d states (see Figure 11b). These facts could mean that when the laser's energy is sufficient to promote an electronic transition from the valence to the lower conduction bands in $BiFeO_3$, a perturbation occurs in the electronic density of the 3d orbitals of the Fe atoms, and consequently, changes in the polarizabilty of iron atoms are manifested as an enhancement in the intensity of only the $A_1$ mode at 216 $cm^{-1}$.

The *R*3*c* symmetry in $BiFeO_3$ permits the development of spontaneous polarization (Ps) along the pseudocubic [111] direction in the cell, due to the displacement of $Bi^{3+}$ and $Fe^{3+}$ cations from their centrosymmetric positions along the 3-fold rotation axis.[91] Also, $BiFeO_3$ can be viewed as a hexagonal cell, instead of the rhombohedral unit cell; for example, using the atomic parameter obtained by Kubel,[93] the sketch in Figure 11c was obtained. The polyhedron around the $Fe^{3+}$ shares an equilateral triangle above and below with the polyhedron around $Bi^{3+}$, as can be seen in Figure 11d (some oxygen atoms of the neighbor hexagonal cells were added to see the atomic environments around the bismuth and iron cations more clearly). The bismuth cations are slightly above the center of their polyhedron due to the stereochemical consequences of the bismuth atom electron lone pair.

When an electronic transition takes place, it can induce a potential energy minimum displacement along the normal coordinate between the ground and the excited electronic states. This condition guarantees the non-nullity of the vibrational overlap integral (Franck–Condon factor) in the resonance Raman effect. Small potential energy minimum displacement provokes enhancements only in the fundamental vibrations.[94] This is the case already discussed at 216 $cm^{-1}$ ($A_{1-3}$) wavenumber, mainly involving Fe atoms. As the mentioned displacement increases, overtones are also observed, and their intensities increase relative to the intensity of the fundamental vibration.[94] That means, in our case where overtones are located between 800 and 1500 $cm^{-1}$, oxygen atoms have the weightiest role in the potential energy minimum displacement when electronic transitions are excited at 2.33 eV. At the same time, the higher the frequency of the fundamental vibration, the higher the intensity for the corresponding overtone; so, potential energy minimum displacement is strongly related to those higher frequency modes.

### 3.6. Mössbauer Spectroscopy.

Figure 12 shows the asymmetric Mössbauer spectra of the $BiFeO_3$ NPs synthesized using tartaric acid and glycine. It can be seen that the magnetic sextet contribution to the experimental spectra (Figure 12a,b,d,e) has slightly broader resonance lines with a noticeable asymmetry. For further discussion on the possible origin of the spectra asymmetry, see the Mössbauer spectroscopy section in the Supporting Information. The corresponding Mössbauer parameters, after fitting the spectra, are presented in Table S2 in the Supporting Information section. For the NPs obtained using tartaric acid (Figure 12a,b) there are two sextets and two doublets, as reported in previous works.[23,24] At 300 K, the two sextets, which can only be present in ferro-, ferri-, or antiferromagnetic materials, have slightly different hyperfine magnetic field (Bhf) values (492 ± 2 and 496 ± 2 kOe) and account for 79% of the relative area of the spectrum. At 77 K, these two Bhf values increase to 522 and 544 kOe, and the two sextets account for 95% of the relative area.

In a group of papers of $^{57}$Fe NMR for $BiFeO_3$ reported by Zalessky et al.,[95−98] the obtained spectra have two peaks of different heights that correspond to two Bhf values measured at 296 K (490.5 and 496 kOe) and at 77 K (538.8 and 546 kOe). The gyromagnetic ratio of $^{57}$Fe nuclei ($\gamma/2\pi$ = 0.138 MHz/kOe) was used to express the NMR frequency values in terms of Bhf values.[95,96] The Mössbauer Bhf values presented in Figure 12a,b agree very well with the ones obtained by $^{57}$Fe NMR and, therefore, support the Zalessky's mathematical model.

The two doublets that account for the 21% of the relative area could be related to (a) the subset of $BiFeO_3$ NPs with the smallest size that have superparamagnetic behavior, (b) Fe on the NP's surface coordinated with $CH_3COO^-$, (c) the formation of $Bi_2Fe_4O_9$ byproduct which has 2 doublets at 300 K.[99] The documented quadrupole splitting for these two doublets in $Bi_2Fe_4O_9$ are 0.94 and 0.38 mm $s^{-1}$ with isomer shifts of 0.24 and 0.36 mm $s^{-1}$.[99,100] These values are similar to our values in Table S2. When the temperature was decreased to 77 K, the relative area also decreased to 5.3% because at this temperature the doublets became two overlapping sextets, as documented by Kostiner et al.[100] According to Park et al.,[23,34] in $BiFeO_3$ NPs of size 14 nm, 66% of the relative area fit to two doublets at 300 K, and they become two sextets at 4.2 K. When the size of the NPs increased to 95 ± 28 nm there were no doublets in the Mössbauer spectrum at 300 K.[23]

It is worthwhile to point out that the intermediate species (Figure 12c) has a low intensity sextet; however, that amount of ferromagnetic iron in the sample is enough to be attracted by a 1.875 × 0.875 × 0.393 in.$^3$ NdBFe magnet. The sextet in the intermediate corresponds to the $BiFeO_3$ already formed; while the doublet corresponds to high spin ferric iron.

The Mössbauer spectrum of the $BiFeO_3$−NPs−PNt with 23 nm of crystallite size (Figure 12d) was fitted to just one sextet with a Bhf value of 494 kOe and 88% of the relative area. On the other hand, the spectrum of the $BiFeO_3$−NPs−PNt of larger crystallite size (67 nm) has broader absorption bands and was fitted to two sextets with Bhf values of 494 and 507 kOe comprising 87% of the relative area (Figure 13e). This difference is probably due to the size, since 67 nm is slightly larger than the period length of 62 nm of the known SSMS for bismuth ferrite while 23 nm is smaller than that period (see Figure 12f).[23]

## 3.7. Vibrating Sample Magnetometry.

*a. $BiFeO_3$ NPs Synthesized Using Tartaric Acid as Ligand.* The magnetization curve ($M$−$H$) for the 26 nm $BiFeO_3$ NPs is shown in Figure 13a for which a noticeable ferromagnetic response is observed, with a saturation magnetization $M_s$ of 3.4 emu $g^{-1}$ and a coercive field $H_c$ of 8 Oe. This behavior is consistent with previous reports of nanosized $BiFeO_3$ particles with mean diameter below 62 nm, whose enhanced ferromagnetism can be ascribed to the effect of breaking periodicity (62 nm) of the spin cycloid structure, characteristic of bulk $BiFeO_3$. A summary of the magnetic properties is shown in Table S3, including comparative data of other works. According to the results of Park et al.,[23] the $H_c$ values increase with the size of $BiFeO_3$ NPs; so, higher $H_c$ values are explained in terms of the higher size of their $BiFeO_3$ NPs (compared with our results). Wang et al.[21] have synthesized $BiFeO_3$ NPs of 60−90 nm using tartaric acid, and the $M$ value (0.34 emu $g^{-1}$) at 15 000 Oe was almost 1 order of magnitude lower than the measured value reported in the present work, which is probably due to their larger size.

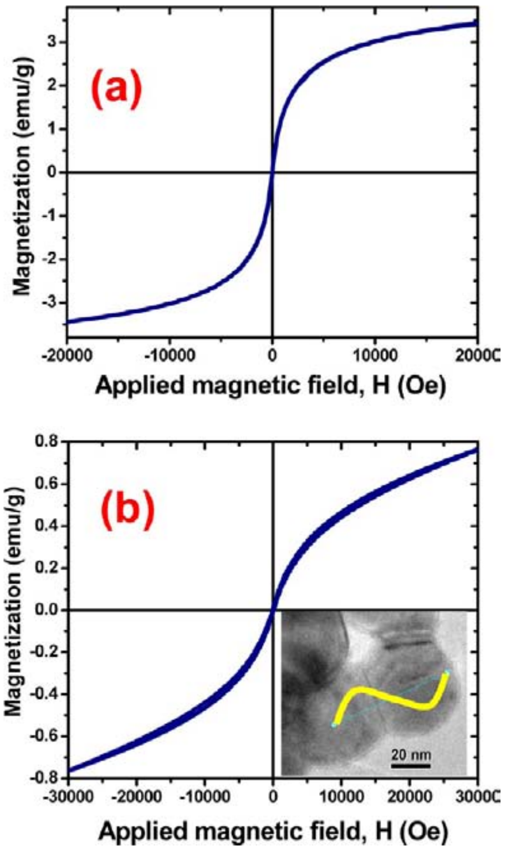

**Figure 13.** Magnetic hysteresis loop of $BiFeO_3$ NPs using tartaric acid (a) and glycine (b) in the synthesis methodology. Inset in part b: HRTEM micrograph of tightly assembled and sintered $BiFeO_3$ NPs forming the porous network. This illustrates the possibility of sintered neighbor NPs with similar crystalline faces. Superimposed on the micrograph, a sketch of the spin cycloid (62 nm) indicated by the yellow sine function graph.

*b. $BiFeO_3$−NPs−PNt Synthesized Using Glycine as Ligand.* For $BiFeO_3$−NPs−PNt with 23 nm of crystallite size, a clear ferro/antiferromagnetic behavior is manifested in the corresponding $M$−$H$ curve (Figure 13b). The observed $M$ value at 20 000 Oe (0.64 emu $g^{-1}$) was ∼5 times lower than that obtained using tartaric acid. This result agrees with the fact that no undesirable secondary magnetic phases are present. In addition, the sintered $BiFeO_3$ nanocrystals forming the porous network (insert in Figure 13b) might promote a partial assembly and continuity of the spin cycloid. This can lead to a dilution effect of the magnetic moment of the powder and, hence, to the significant reduction observed for $M$ (0.64 emu $g^{-1}$). The strong tendency of preferential alignment during the nanocrystal aggregation has been observed and theoretically supported in different oxides.[101,102] This preferential alignment has been explained in terms of interparticle interaction forces and/or external forces.[101] The nature of the ordering physical field-forces can be (i) electric, (ii) magnetic, and/or (iii) higher order multipole moments interaction of the crystalline faces.[101] It is important to highlight that the contact between parallel faces of the hexagonal nanocrystals (insert in Figure 13b) suggests the contact between the faces (10−10), (01−10), or (−1100) of the hexagonal unit cell.[93] The mutual alignment of NPs of identical crystal faces is one of the main arguments used in the literature[101] to explain the formation of three-dimensional NPs arrays (mesocrystals).

In turn, this preferential alignment tendency of crystallite aggregates is different from what takes place when $BiFeO_3$ nanopowders are obtained using tartaric acid (see Figure 5a). In such a case, a mixture of $BiFeO_3$ and $Bi_2O_3$ is formed in the synthesis (Figure 1a). Then, the direct contact between $BiFeO_3$ particles can be partially hindered, and the driving forces for the preferential alignment are minimized. Finally, the $BiFeO_3$ nanocrystallites rinsed with acetic acid do not have strong sintering and exhibit slightly rounded surfaces probably because of chemical etching.

Previous works in the literature that have used EPR for $BiFeO_3$ characterization always contained $Bi_2Fe_4O_9$ as impurity in considerable amounts.[103] To the best of our knowledge, this is the first time that EPR parameters (i.e., resonance field, *g*-factor, and signal width) are reported for high purity $BiFeO_3$.

## CONCLUSIONS

In summary, an integral analysis and discussion of the synthesis pathways and structural, morphological, optical, and magnetic attributes of two sorts of $BiFeO_3$ NPs are provided in this paper.

The use of tartaric acid as ligand in the $BiFeO_3$ synthesis produces nanopowders with crystallite size around 26 nm. The main byproduct formed is the metastable $\beta$-$Bi_2O_3$ phase, which could be efficiently removed with $CH_3COOH$. Also, some traces of tiny $Bi_2Fe_4O_9$ NPs of about 5 nm were found in the same sample. The thorough characterization of these $BiFeO_3$ NPs led us to the following relevant findings: (i) the presence of both types of electronic transitions (direct and indirect, located in the visible region) and (ii) a remarkable selective enhancement in the intensity of the $BiFeO_3$ $A_1$ mode (216 $cm^{-1}$), as a consequence of the resonance Raman effect. Both i and ii were observed and discussed for the first time in this work.

When glycine is used as ligand, a porous $BiFeO_3$ network, composed of tightly assembled and sintered nanocrystallites of high purity, was obtained. The following two important issues have not been addressed before in the literature: (i) There is an intermediate produced during the synthesis that could be the key species to generate high purity $BiFeO_3$. This intermediate is a porous network of nanoparticles smaller than 10 nm, mainly formed by $BiFeO_3$, an amorphous phase, and probably a nonstoichiometric $BiFeO_{3-x}$. This porous array formation is explained on the basis of the chemical reaction that involves an explosive glycine−nitrates mixture. (ii) There is a clear correlation between the singular morphology of the $BiFeO_3$−NPs−PNt and its magnetic properties, which are significantly different from those of its analogue derived from tartaric acid.

The $BiFeO_3$ nanoparticles, prepared using tartaric acid, have lower resonance field (and higher *g*-factor) than that of the $BiFeO_3$−NPs−PNt; this is the first report of the main EPR parameters for high purity $BiFeO_3$ nanopowders.

## ASSOCIATED CONTENT

### Ⓢ Supporting Information

Additional figures and tables. Video of HRTEM images showing the interaction of the electron beam with 5 nm $Bi_2Fe_4O_9$ NPs. This material is available free of charge via the Internet at http://pubs.acs.org.

## AUTHOR INFORMATION

### Corresponding Author

*E-mail: david@servidor.unam.mx.

### Notes

The authors declare no competing financial interest.

## ACKNOWLEDGMENTS

The research leading to these results has received funding from the European Community Seven Framework Programme (FP7-NMP-2010-EU-MEXICO) and CONACYT, (*BisNano*), under Grants 263878 and 125141, respectively. D.D. wants to express his gratitute to DGAPA-UNAM and CONACyT, for the financial support through (PAPIIT IN 101009) and (SEP-CB-132094) projects. J.-L.O.-Q. deeply thanks CONACyT for his M.Sc. scholarship. I.Z.-D. thanks the postdoctoral fellowship awards from ICyTDF, CONACyT, and *BisNano*. Authors thank Mr. Luis Rendón for the HRTEM experimental work and Dr. José Elizalde-Galindo from UACJ for the VSM measurements. Likewise, the authors wish to acknowledge Dr. Edilso Reguera-Ruiz, from CICATA Unidad Legaria of the Instituto Politécnico Nacional, for allowing access to Raman scattering spectrometer and TGA measurements and to Dr. Roberto Escudero-Derat from IIM-UNAM for the measurement of the magnetic susceptibility vs temperature. Thanks to Dr. Mou and Umapada Pal from Instituto de Física at Benemérita Universidad Autónoma de Puebla, and M.Sc. Juan Rizo from UNAM, for their careful manuscript language review. Finally, the authors also thank Dr. Vicente Garibay, head of the Ultra High Resolution Electron Microscopy facilities from Instituto Mexicano del Petróleo where the HRTEM work was performed.

## REFERENCES

(1) Khikhlovskyi, V. V. M.Sc. Thesis, Zernike Institute for Advanced Materials, University of Groningen, Groningen, Germany, 2010.

(2) Zang, Y.; Xie, D.; Wu, X.; Chen, Y.; Lin, Y.; Li, M.; Tian, H.; Li, X.; Li, Z.; Zhu, H.; Ren, T.; Plant, D. *Appl. Phys. Lett.* **2011**, *99*, 132904.

(3) Yang, S. Y.; Seidel, J.; Byrnes, S. J.; Shafer, P.; Yang, C. H; Rossell, M. D.; Yu, P.; Chu, Y. H.; Scott, J. F.; Ager, J. W.; Martin, L. W.; Ramesh, R. *Nat. Nanotechnol.* **2010**, *5*, 143−147.

(4) Catalan, G.; Scott, J. F. *Adv. Mater.* **2009**, *21*, 2463.

(5) Maruyama, K.; Kondo, M.; Singh, S. K.; Ishiwara, H. *Fujitsu Sci. Tech. J.* **2007**, *43*, 502−507.

(6) Wang, J.; Scholl, A.; Zheng, H.; Ogale, S. B.; Viehland, D.; Schlom, D. G.; Spaldin, N. A.; Rabe, K. M.; Wuttig, K. M.; Mohaddes, L.; Neaton, J.; Waghmare, U.; Zhao, T.; Ramesh, R. *Science* **2005**, *307*, 1203.

(7) Yang, J.; Li, X.; Zhou, J.; Tang, Y.; Zhang, Y.; Li, Y. *J. Alloys Compd.* **2011**, *509*, 9271−9277.

(8) Xian, T.; Yang, H.; Dai, J. F.; Wei, Z. Q.; Ma, J. Y.; Feng, W. J. *Mater. Lett.* **2011**, *65*, 1573−1575.

(9) Gao, F.; Chen, X.; Yin, K.; Dong, S.; Ren, Z.; Yuan, F.; Yu, T.; Zou, Z.; Liu, J. *Adv. Mater.* **2007**, *19*, 2889−2892.

(10) Huo, Y.; Jin, Y.; Zhang, Y. *J. Mol. Catal. A: Chem.* **2010**, *331*, 15−20.

(11) Wang, N.; Zhu, L.; Lei, M.; She, Y.; Cao, M.; Tang, H. *ACS Catal.* **2011**, *1*, 1193−1202.

(12) Deng, J.; Banerjee, S.; Mohapatra, S. K.; Smith, Y. R.; Misra, M. *J. Fundam. Renewable Energy Appl.* **2011**, *1*, ArticleID R101204.

(13) Silva, J.; Reyes, A.; Esparza, H.; Camacho, H.; Fuentes, L. *Integr. Ferroelectr.* **2011**, *126*, 47−59.

(14) Cheng, Z. X.; Wang, X. L.; Du, Y.; Dou, S. X. *J. Phys. D: Appl. Phys.* **2010**, *43*, 242001.

(15) Jurca, B.; Paraschiv, C.; Ianculescu, A.; Carp, O. *J. Therm. Anal. Calorim.* **2009**, *97*, 91−98.

(16) Mashino, T.; Kimura, S.; Shigeoka, D.; Hiroki, T.; Katayanagi, H.; Moro, Y.; Ichiyanagi, Y. *J. Phys.: Conf. Ser.* **2010**, *200*, 072041.

(17) Szafraniak, I.; Połomska, M.; Hilczer, B.; Pietraszko, A.; Kepinski, L. *J. Eur. Ceram. Soc.* **2007**, *27*, 4399−4402.

(18) Kumar, M. M.; Palkar, V. R.; Srinivas, K.; Suryanarayana, S. V. *Appl. Phys. Lett.* **2000**, *76*, 2764−2766.

(19) Prado, J.; Villafuerte, M. E.; Fuentes, L.; Morán, E. *Mater. Res. Bull.* **2009**, *44*, 1734−1737.

(20) Lebeugle, D.; Colson, D.; Forget, A.; Viret, M.; Bonville, P.; Marucco, J. F.; Fusil, S. *Phys. Rev. B* **2007**, *76*, 024116.

(21) Wang, X.; Zhang, Y.; Wu, Z. *Mater. Lett.* **2010**, *64*, 486−488.

(22) Hu, Y.; Fei, L.; Zhang, Y.; Yuan, J.; Wang, Y.; Gu, H. *J. Nanomater.* **2011**, Article 797639.

(23) Park, T.; Papaefthymiou, G. C.; Viescas, A. J.; Moodenbaugh, A. R.; Wong, S. S. *Nano Lett.* **2007**, *7*, 766−772.

(24) Park, T. Multifunctional iron-based metal oxide nanostructured materials: Synthesis, characterization, and properties. Dissertation, Stony Brook University, Stony Brook, NY, 2007, pp 39−63.

(25) Chen, P.; Xu, X.; Koenigsmann, C.; Santulli, A. C.; Wong, S. S.; Musfeldt, J. L. *Nano Lett.* **2010**, *10*, 4526−4532.

(26) Yang, Y.; Sun, J. Y.; Zhu, K.; Liu, Y. L.; Chen, J.; Xing, X. R. *Physica B* **2009**, *404*, 171−174.

(27) Jaiswal, A.; Das, R.; Maity, T.; Vivekanand, K.; Adyanthaya, S.; Poddar, P. *J. Phys. Chem. C* **2010**, *114*, 12432−12439.

(28) Kothari, D.; Raghavendra, V.; Sathe, V. G.; Gupta, A.; Banerjee, A.; Awasthi, A. M. *J. Magn. Magn. Mater.* **2008**, *320*, 548−552.

(29) Fukumura, H.; Harima, H.; Kisoda, K.; Tamada, M.; Noguchi, Y.; Miyayama, M. *J. Magn. Magn. Mater.* **2007**, *310*, 367−369.

(30) Xu, Q.; Zai, H.; Wu, D.; Qiu, T.; Xu, M. X. *Appl. Phys. Lett.* **2009**, *95*, 112510.

(31) Lobo, R. P.; Moreira, L. R.; Lebeugle, D.; Colson, D. *Phys. Rev. B* **2007**, *76*, 172105.

(32) Singh, M. K.; Jang, H. M.; Ryu, S.; Jo, M. *Appl. Phys. Lett.* **2006**, *88*, 042907.

(33) Yuan, G. L.; Or, S. W.; Chan, H. L.; Liu, Z. G. *J. Appl. Phys.* **2007**, *101*, 024106.

(34) Ramirez, M. O.; Krishnamurthi, M.; Denev, S.; Kumar, A.; Yang, S. Y.; Chu, Y. H.; Saiz, E.; Seidel, J.; Pyatakov, A. P; Bush, A.; Viehland, D.; Orenstein, J.; Ramesh, R.; Gopalan, V. *Appl. Phys. Lett.* **2008**, *92*, 022511.

(35) Smith, E.; Dent, G. *Modern Raman Spectroscopy—A Practical Approach*, 1st ed.; John Wiley & Sons Ltd: Chicester, U.K., 2005; Chapters 1, 3, 4.

(36) Da Silva, K. L.; Menzel, D.; Feldhoff, A.; Kübel, C.; Bruns, M.; Paesano, A.; Düvel, A.; Wilkening, M.; Ghafari, M.; Hahn, H.; Litterst, F. J.; Heitjans, P.; Becker, K. D.; Sepelak, V. *J. Phys. Chem. C* **2011**, *115*, 7209−7217.

(37) Prado-Gonjal, J.; Ávila, D.; Villafuerte-Castrejón, M. E.; González-García, F.; Fuentes, L.; Gómez, R. W.; Pérez-Mazariego, J. L.; Marquina, V.; Morán, E. *Solid State Sci.* **2011**, *13*, 2030−2036.

(38) Joshi, U. A.; Jang, J. S.; Borse, P. H.; Lee, J. S. *Appl. Phys. Lett.* **2008**, *92*, 242106.

(39) Bhushan, B.; Das, D.; Priyam, A.; Vasanthacharya, N. Y.; Kumar, S. *Mater. Chem. Phys.* **2012**, *135*, 144−149.

(40) Kumar, M.; Gajbhiye, N. S. *J. Am. Ceram. Soc.* **2012**, *95*, 3678−3682.

(41) Tang, P.; Chen, H.; Cao, F.; Pan, G.; Xu, M.; Wang, K.; Tong, Y. *Appl. Mech. Mater.* **2012**, *110−116*, 1912−1917.

(42) Arora, M.; Sati, P. C.; Chauhan, S.; Chokker, K.; Panwar, A. K.; Kumar, M. *J. Supercond. Novel Magn.* **2013**, *26*, 443−448.

(43) Wang, X.; Zhang, Y.; Wu, Z. *Mater. Lett.* **2010**, *64*, 486−488.

(44) Wang, X.; Lin, Y.; Jiang, J. *Adv. Mater. Res.* **2011**, *152−153*, 81−85.

(45) Zhao, Y.; Miao, J.; Zhang, X.; Chen, Y.; Xu, X. G.; Jiang, Y. *J. Mater. Sci: Mater. Electron.* **2012**, *23*, 180−184.

(46) Takahashi, K.; Kida, N.; Tonouchi, M. *Phys. Rev. Lett.* **2006**, *96*, 117402.

(47) Basu, S. R.; Martin, L. W.; Chu, Y. H.; Gajek, M.; Ramesh, R.; Rai, R. C.; Xu, X.; Musfeldt, J. L. *Appl. Phys. Lett.* **2008**, *92*, 091905.

(48) Fruth, V.; Tenea, E.; Gartner, M.; Anastasescu, M.; Berger, D.; Ramer, R.; Zaharescu, M. *J. Eur. Ceram. Soc.* **2007**, *27*, 937−940.

(49) Jiang, K.; Zhu, J. J.; Wu, J. D.; Sun, J.; Hu, Z. G.; Chu, J. H. *ACS Appl. Mater. Interfaces* **2011**, *3*, 4844−4852.

(50) Hancock, R. D; Cukrowsky, I.; Baloyi, J.; Mashishi, J. *J. Chem. Soc., Dalton Trans.* **1993**, 2895−2899.

(51) Smith, R. M.; Martell, A. *Critical Stability Constants*; Plenum Press: New York, 1977; Vol. *3*, pp 128, 161−163; Vol. *5*, pp 393−395; Vol. *6*, pp 341, 343.

(52) Hwang, C. C.; Tsai, J. S.; Huang, T. H. *Mater. Chem. Phys.* **2005**, *93*, 330−336.

(53) Blower, S. K.; Greaves, C. *Acta Crystallogr., Sect. C* **1988**, *44*, 587−589.

(54) Kothai, V.; Ranjan, R. *Bull. Mater. Sci.* **2012**, *35*, 157−161.

(55) Holleman, A. F.; Wiberg, E. *Inorganic Chemistry*; Academic Press: San Diego, 2001; p 771.

(56) Näslund, J.; Persson, I.; Sandström, M. *Inorg. Chem.* **2000**, *39*, 4012−4021.

(57) Miersch, L.; Schlesinger, M.; Troff, R.; Schalley, C.; Rüffer, T.; Lang, H.; Zahn, D.; Mehring, M. *Chem.—Eur. J.* **2011**, *17*, 6985−6990.

(58) Christensen, A.; Lebech, B. *Dalton Trans.* **2012**, *41*, 1971−1980.

(59) Henrya, N.; Mentre, O.; Abraham, F.; MacLean, E. J.; Roussel, P. *J. Solid State Chem.* **2006**, *179*, 3087−3094.

(60) Thurston, J. H.; Swenson, D. C.; Messerle, L. *Chem. Commun.* **2005**, 4228−4230.

(61) Sagatys, D. S.; Oreilly, E. J.; Patel, S.; Bott, R. C.; Lynch, D. E.; Smith, G.; Kennard, C. *Aust. J. Chem.* **1992**, *45*, 1027−1034.

(62) Yokoi, H.; Mitani, T.; Mori, Y.; Kawata, S. *Chem. Lett.* **1994**, *2*, 281−284.

(63) Timberlake, C. F. *J. Chem. Soc.* **1964**, *0*, 1229−1240.

(64) Nyquist, R. A.; Kagel, R. O. *Handbook of Infrared and Raman Spectra of Inorganic Compounds and Organic Salts*; Academic Press: San Diego, 1997, Vol. *4*; p 133.

(65) Taylor, P.; Sunder, S.; Lopata, V. J. *Can. J. Chem.* **1984**, *62*, 2863−2873.

(66) Chick, L. A.; Pederson, L. R.; Maupin, G. D.; Bates, J. L.; Thomas, L. E.; Exarhos, G. J. *Mater. Lett.* **1990**, *10*, 6−12.

(67) Pine, T.; Lu, X.; Mumm, D.; Samuelsen, G. S.; Brouwer, J. *J. Am. Ceram. Soc.* **2007**, *90*, 3735−3740.

(68) Valefi, M.; Falamaki, C.; Ebadzadeh, T.; Solati, M. *J. Am. Ceram. Soc.* **2007**, *90*, 2008−2014.

(69) Yildiz, Ö.; Soydan, A. M.; Ata, A.; Tunaboylu, B.; Akin, D.; Ipcizade, E. F. *Acta Phys. Pol., A* **2012**, *123*, 432−435.

(70) Hwang, C. C.; Wu, T. Y.; Wan, J.; Tsai, J. S. *Mater. Sci. Eng., B* **2004**, *111*, 49−56.

(71) Miersch, L.; Rüffer, T.; Schlesinger, M.; Lang, H.; Mehring, M. *Inorg. Chem.* **2012**, *51*, 9376−9384.

(72) Mazumder, R.; Devi, P. S.; Bhattacharya, D.; Choudhury, P.; Sen, A.; Raja, M. *Appl. Phys. Lett.* **2007**, *91*, 062510.

(73) Jurca, B.; Paraschiv, C.; Ianculescu, A.; Carp, O. *J. Therm. Anal. Calorim.* **2009**, *97*, 91−98.

(74) Zhang, Q.; Gong, W.; Wang, J.; Ning, X.; Wang, Z.; Zhao, X.; Ren, W.; Zhang, Z. *J. Phys. Chem. C* **2011**, *115*, 25241−25246.

(75) Buffat, P. A. *Phil. Trans. R. Soc., A* **2003**, *361*, 29−295.

(76) Wagner, J. B.; Willinger, M. G.; Müller, J. O.; Su, D. S.; Schlögl, R. *Small* **2006**, *2*, 230−234.

(77) Beer, A.; Kofman, R.; Phillipp, F.; Lereah, Y. *Phys. Rev. B* **2006**, *74*, 224111.

(78) Bhushan, B.; Wang, Z.; Tol, J. V.; Dalal, N. S.; Basumallick, A.; Vasanthacharya, N. Y.; Kumar, S.; Das, D. *J. Am. Ceram. Soc.* **2012**, *95*, 1985−1992.

(79) Joshi, U. A.; Jang, J. S; Borse, P. H.; Lee, J. S. *Appl. Phys. Lett.* **2008**, *92*, 242106.

(80) Arora, M.; Chauhan, P. C. S. S.; Chhoker, S.; Panwar, A. K.; Kumar, M. *J. Supercond. Novel Magn.* **2013**, *26*, 443−448.

(81) Seidel, J.; Luo, W.; Suresha, S. J.; Nguyen, P.-K.; Lee, A. S.; Kim, S. Y.; Yang, C. H.; Pennycook, S. J.; Pantelides, S. T.; Scott, J. F.; Ramesh, R. *Nat. Commun.* **2012**, *3*, 799.

(82) Kumar, A.; Rai, R.; Podraza, N. K.; Denev, S.; Ramirez, M.; Chu, Y. H.; Martin, L. W.; Ihlefeld, J.; Heeg, T.; Schubert, J.; Schlom, D. G.;

Orenstein, J.; Ramesh, R.; Collins, R. W.; Musfeldt, J. L.; Gopalan, V. *Appl. Phys. Lett.* **2008**, *92*, 121915.
(83) Ihlefeld, J. F.; Podraza, N. J.; Liu, Z. K.; Rai, R. C.; Xu, X.; Heeg, T.; Chen, Y. B.; Li, J.; Collins, R. W.; Musfeldt, J. L.; Pan, X. Q.; Schubert, J.; Ramesh, R.; Schlom, D. G. *Appl. Phys. Lett.* **2008**, *92*, 142908.
(84) Palai, R.; Katiyar, R. S.; Schmid, H.; Tissot, P.; Clark, S. J.; Robertson, J.; Redfern, S. A.; Catalan, G.; Scott, J. F. *Phys. Rev. B* **2008**, *77*, 014110.
(85) Dong, H.; Wu, Z.; Wang, S.; Duan, W.; Li, J. *Appl. Phys. Lett.* **2013**, *102*, 072905.
(86) Fu, Z.; Yin, Z. G.; Chen, N. F.; Zhang, X. W.; Zhang, H.; Bai, Y. M.; Wu, J. L. *Phys. Status Solidi RRL* **2012**, *6*, 37−39.
(87) Gao, F.; Yuan, Y.; Wang, K. F.; Chen, X. Y.; Chen, F.; Liu, J. M.; Ren, Z. F. *Appl. Phys. Lett.* **2006**, *89*, 102506.
(88) Gujar, T. P.; Shinde, V. R.; Lokhande, C. D. *Mater. Chem. Phys.* **2007**, *103*, 142−146.
(89) Wang, H.; Zheng, Y.; Cai, M.-Q.; Huang, H.; Chan, H. L. W. *Solid State Commun.* **2009**, *149*, 641−644.
(90) Kamba, S.; Nuzhnyy, D.; Savinov, M.; Šebek, J.; Petzelt, J.; Prokleška, J.; Haumont, R.; Kreisel, J. *Phys. Rev. B* **2007**, *77*, 024403.
(91) Porporati, A. A.; Tsuji, K.; Valant, M.; Axelsson, A. K.; Pezzottia, G. *J. Raman Spectrosc.* **2010**, *41*, 84−87.
(92) Liu, K.; Fan, H.; Ren, P.; Yang, C. *J. Alloys Compd.* **2011**, *509*, 1901−1905.
(93) Kubel, F.; Schmid, H. *Acta Crystallogr., Sect. B* **1990**, *46*, 698−702.
(94) Kim, H.; Kosuda, K. M.; Van Duyne, R.; Stair, P. *Chem. Soc. Rev.* **2010**, *39*, 4820−4844.
(95) Zalessky, A. V.; Frolov, A. A.; Khimich, T. A.; Bush, A. A.; Pokatilov, V. S.; Zvezdin, A. K. *Europhys. Lett.* **2000**, *50*, 547−551.
(96) Zalesski, A. V.; Zvezdin, A. K.; Frolov, A. A.; Bush, A. A. *JETP Lett.* **2000**, *71*, 465−468.
(97) Zalesski, A. V.; Frolov, A. A.; Zvezdin, A. K.; Gippius, A. A.; Morozova, E. N.; Khozeev, D. F.; Bush, A. S.; Pokatilov, V. S. *JETP Lett.* **2002**, *95*, 101−105.
(98) Khozeev, D. F.; Zalessky, A. V.; Gippius, A. A.; Morozova, E. N.; Bush, A. A. *Physica B* **2003**, *329−333*, 848−849.
(99) Park, T.; Papaefthymiou, G. C.; Moodenbaugh, A. R.; Mao, Y.; Wong, S. S. *J. Mater. Chem.* **2005**, *15*, 2099−2105.
(100) Kostiner, E.; Shoemaker, G. L. *J. Solid State Chem.* **1971**, *3*, 186−189.
(101) Song, R. Q.; Cölfen, H. *Adv. Mater.* **2010**, *22*, 1301−1330.
(102) Ponzoni, C.; Rosa, R.; Cannio, M.; Buscaglia, V.; Finocchio, E.; Nanni, P.; Leonelli, C. *J. Alloys Compd.* **2013**, *558*, 150−159.
(103) Szafraniak-Wiza, I.; Bednarski, W.; Waplak, S.; Hilczer, B.; Pietraszko, A.; Kepinski, L. *J. Nanosci. Nanotechnol.* **2009**, *9*, 3246−3251.